Two dimensional plastic waves in quasi rate independent viscoplastic materials

M.V. Mićunović[*]   C. Albertini[†]   A. Grillo[‡]

I. Muha[§]   G. Wittum[¶]   L. Kudrjavceva[‖]

Abstract

The subject of this work is an analysis of the experimental bi-axial Hopkinson bar technique when such a device consists of a cruciform tensile specimen surrounded by four very long elastic bars. Unlike commonly applied by-pass analysis which attempts to draw conclusions from behaviour of elastic bars we attempt to take into account real plastic waves inside the specimen with few hundreds of reflections. A quasi rate-independent as well as a more general rate-dependent tensor function model for ASME 537 steel are applied. Plastic wave speeds non-existent in tradi-tional elasto-viscoplasticity are analyzed. Some preliminary nu-merical results for symmetric and non-symmetric loading cases valid for initial and subsequent elastic ranges are given.

Keywords: 2D Hopkinson bar, cruciform specimen, quasi rate independent materials

[*]University of Kragujevac, Serbia, e-mail: mmicun@kg.ac.rs
[†]JRC CEC, Ispra, Italy
[‡]G-CSC, Goethe University of Frankfurt, Germany
[§]G-CSC, Goethe University of Frankfurt, Germany
[¶]G-CSC, Goethe University of Frankfurt, Germany
[‖]State University of Novi Pazar, Serbia

1 Introduction

The motivation for this paper [1] lies in experimental evidence achieved in the Laboratory for dynamic testing of JRC, Ispra [1] where the unique biaxial cruciform specimen (cf. Fig. 1) based Hopkinson bar has been devised and used. The testing program has shown that plane waves may be split by means of homogeneous dynamic deformation until fracture. The specimen was made of steel $ASME$ 537. Due to very small dimensions of the cruciform specimen used and measurement technique performed outside the specimen a careful analysis of plastic waves inside the specimen is needed. In view of such an evidence the analysis of plastic waves from [2] is extended here to the two-dimensional case. This includes all the theoretical assumptions, the analysis of wave equation and methodology of [2].

Details of the unique Hopkinson bar device built in JRC, Ispra are given elsewhere.

2 Evolution equations

It is a known fact that initial yield stress under dynamic loading depends on strain rate or stress rate: at higher stress rates the initial stress yield is larger. On the other hand, the phenomenon of delayed yielding inherent to some metals and alloys is observed [4]: stress under dynamic loading exceeds its static value and plasticity starts after a certain time called delay time. Let plastic deformation commence at time t^*. Denote by Y_0 the initial equivalent static yield stress, and by $Y = Y(D_t\sigma_{eq} \mid t = t^*)$ theinitial equivalent dynamic yield stress. Then, the accumulated plastic strain is governed by corresponding constitutive equation having the following form [2]:

$$\varepsilon_{eq}^p(t) = \int_0^t J(t - \tau)\, D_\tau\sigma_{eq}(\tau)\, d\tau.$$

In other words,

$$D_t\varepsilon_{eq}^p(t) = J(0)\, D_t\sigma_{eq}(t).$$

---

[1]The majority of this text was presented at the ESMC2009, Lisbon, Portugal.

The upper view of the cruciform specimen

MEASUREMENTS

1. Change of thickness
2. Distributed forces
3. In-plane displacements
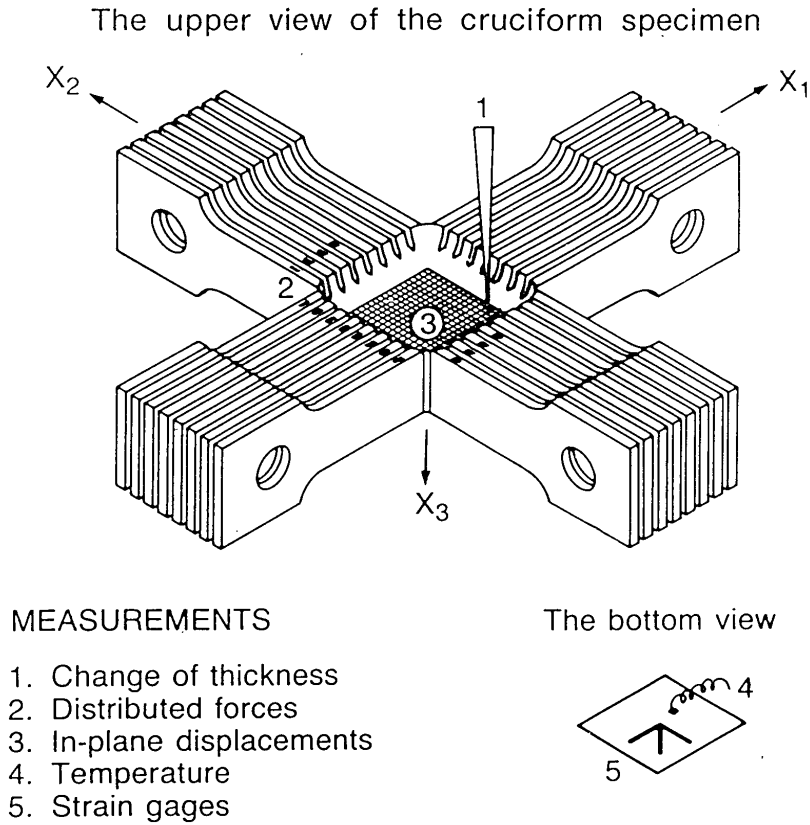4. Temperature
5. Strain gages

The bottom view

Figure 1: Biaxial Hopkinson in JRC, Ispra, Italy

with the kernel $J(t - \tau) = 0$ if $\tau < t^*$ and $J(t - \tau) = \exp(-\mathcal{M})$ for $\tau \geq t^*$. Here $\mathcal{M}$ is an *"universal"* constant (which means the same for uniaxial tension, biaxial tension and shear) introduced and determined for AISI 316H steel in [3] as well as for ASME 537 steel in [1] within a very wide range of strain rates from $10^{-3}[s^{-1}]$ to $100\,[s^{-1}]$. Let us note that for convenience the material time derivative is here denoted by $D_t \mathcal{A} \equiv D\mathcal{A}/Dt$.

In this paper a simplest version of endochronic evolution is used permitting scaling of plastic strain rate, being very useful for calibration from low to almost impact strain rates. Let us introduce invariants: $s_1 = tr\mathbf{S}$, $s_2 = tr\mathbf{S}_D^2$ of the second Piola-Kirchhoff stress tensor deviator related to the intermediate local reference configuration. Then, the model to be used here is described by the following tensor representation:

$$\mathbf{D}_P = \Lambda \sum_{\alpha=1}^{2} \Gamma_\alpha(s_1, s_2)\mathbf{H}_\alpha, \tag{1}$$

with a scalar coefficient Λ responsible for rate dependence:

$$\Lambda = \eta(\bar{\sigma} - Y)(\bar{\sigma}/Y_0 - 1)^\lambda \exp(-M)\, D\bar{\sigma}/Dt, \tag{2}$$

Here the tensor generators and the scalar coefficients are:

$$\mathbf{H}_1 = \frac{[\mathbf{S} - (1/3)\,\mathbf{1}\,tr\mathbf{S}]}{Y_0} \equiv \frac{\mathbf{S}_\mathrm{D}}{Y_0}, \quad \mathbf{H}_2 = \left(\mathbf{S}_D^2\right)_D/Y_0^2,$$

$$\Gamma_1 = a_1 + a_2 s_1 + a_3 s_2, \qquad \Gamma_2 = -3a_2/2,$$

whereas $\eta(x)$ - the Heaviside's function, λ - a material constant. The stresses Y and Y_0 are explained above. At first sight (1) seems to be rate independent. However, the rate dependence appears in stress rate dependent value of the initial yield stress Y, which has a triggering role for inelasticity onset. The model is named as *"quasi rate independent"* .

3   Wave equations

According to experimental evidence [1] we assume that shears are neglected i.e. that in the Kröner's decomposition rule $\mathbf{F} = \mathbf{F}^{el}\mathbf{F}^{pl}$ elastic

and plastic distortions are diagonal leading to

$$\mathbf{F} = \begin{pmatrix} 1 + \varepsilon_1 & 0 & 0 \\ 0 & 1 + \varepsilon_2 & 0 \\ 0 & 0 & 1 + \varepsilon_3 \end{pmatrix},$$

$$\mathbf{F}^{el} = \begin{pmatrix} 1 + \varepsilon_1^{el} & 0 & 0 \\ 0 & 1 + \varepsilon_2^{el} & 0 \\ 0 & 0 & 1 + \varepsilon_3^{el} \end{pmatrix}, \tag{3}$$

$$\mathbf{F}^{pl} = \begin{pmatrix} 1 + p_1 & 0 & 0 \\ 0 & 1 + p_2 & 0 \\ 0 & 0 & 1 + p_3 \end{pmatrix}.$$

The shape of the specimen shown on Figure 1. dictates plane stress. On the other hand, although the approach covers finite strains, the present analysis is restricted to inelastic behaviour far from necking. This means that plastic incompressibility may be assumed such that $p_3 = -1 + (1 + p_1)^{-1}(1 + p_2)^{-1}$. Then we have to consider a 2-D case.

Let us reserve the value of upper or lower index "A" taking values 1 and 2. Now, making use of evolution equations (1), geometric relations $\partial \varepsilon_A / \partial t = \partial V_A / \partial Z_A$, and momentum balance equations we arrive at wave equations (with velocity in-plate components $\{V_1, V_2\}$)

$$\frac{\partial \mathcal{U}}{\partial t} - \sum_{A=1}^{2} \mathbb{A}^A(\mathcal{U}) \frac{\partial \mathcal{U}}{\partial Z_A} = 0. \tag{4}$$

Here $\mathcal{U} = \{V_1, V_2, \varepsilon_1, \varepsilon_2, p_1, p_2\}^T$ is a state vector which describes completely viscoplastic acceleration wave. Like in [2], a solution of (4) is assumed to have the form

$$\mathcal{U} = \mathcal{U}_0 \exp i \left(n_1 Z_1 + n_2 Z_2 - ct \right),$$

where c is a wave speed and wave propagation takes place in the direction $\{n_1, n_2\}$. This gives rise to the Christoffel's equation $(-c\mathbb{I} - \mathbb{A})\mathcal{U} = 0$, leading to the characteristic equation

$$\det(-c\mathbb{I} - \mathbb{A}) = 0. \tag{5}$$

Since the (6×6) acoustic tensor has the form $\mathbb{A} = \sum_{A=1,2} \mathbb{A}^A (\mathcal{U}^{\#}) n_A,$ with $\mathcal{U}^{\#} = \{\varepsilon_1, \varepsilon_2, p_1, p_2\}$, we obtain like in [2] that plastic speeds are not constant unless for small strain case $\|\mathcal{U}^{\#}\| \ll 1$ (i.e. for strains of few percents). This is contrary to the traditional viscoplastic wave theory (cf. [4]) where only elastic waves with constant wave speeds exist due to the fact that plastic stretching $\mathbf{D}_P$ in traditional setting depends on stress and strain but not on stress rate as in quasi rate independent theory.

3.1 Details of wave equations

The equations (4) with first time derivatives may be transformed into the second time derivatives based equations by means of new state vector $\mathcal{U}^u = \{u_1, u_2, \varepsilon_1, \varepsilon_2, p_1, p_2\}$, and two matrices $\mathbb{I}^2 = diag\{1, 1, 0, 0, 0, 0\}$ and $\mathbb{I}^1 = diag\{0, 0, 1, 1, 1, 1\}$. Then the wave equations read:

$$\mathbb{I}^2 \frac{\partial^2 \mathcal{U}^u}{\partial t^2} + \mathbb{I}^1 \frac{\partial \mathcal{U}^u}{\partial t} - \sum_{A=1,2} \mathbb{A}^{uA}(\mathcal{U}^{\#}) \frac{\partial \mathcal{U}^{\#}}{\partial Z_A} - \mathbb{B} \frac{\partial \mathcal{V}}{\partial t} = 0, \tag{6}$$

with the new divergence-like vector

$$\mathcal{V} := \{\frac{\partial U_1}{\partial Z_1}, \frac{\partial U_2}{\partial Z_2}, 0, 0, 0, 0\}^T$$

Here the non-dimensional displacements are introduced by means of $\{V_1, V_2\} = \partial \{U_1, U_2\} / \partial t$. The above new three matrices read:

$$\mathbb{A}^{u1} = \begin{pmatrix} 0 & 0 & c_{01}^2 a_{11} & c_{01}^2 a_{21} & c_{01}^2 b_{11} & c_{01}^2 b_{21} \\ 0 & 0 & 0 & 0 & 0 & 0 \\ 0 & 0 & 0 & 0 & 0 & 0 \\ 0 & 0 & 0 & 0 & 0 & 0 \\ 0 & 0 & 0 & 0 & 0 & 0 \\ 0 & 0 & 0 & 0 & 0 & 0 \end{pmatrix} \tag{7}$$

$$\mathbb{A}^{u2} = \begin{pmatrix} 0 & 0 & 0 & 0 & 0 & 0 \\ 0 & 0 & c_{02}^2 a_{12} & c_{02}^2 a_{22} & c_{02}^2 b_{12} & c_{02}^2 b_{22} \\ 0 & 0 & 0 & 0 & 0 & 0 \\ 0 & 0 & 0 & 0 & 0 & 0 \\ 0 & 0 & 0 & 0 & 0 & 0 \\ 0 & 0 & 0 & 0 & 0 & 0 \end{pmatrix} \tag{8}$$

$$\mathbb{B} = \begin{pmatrix} 0 & 0 & 0 & 0 & 0 & 0 \\ 0 & 0 & 0 & 0 & 0 & 0 \\ 1 & 0 & 0 & 0 & 0 & 0 \\ 0 & 1 & 0 & 0 & 0 & 0 \\ \eta a_{51} & \eta a_{52} & 0 & 0 & 0 & 0 \\ \eta a_{61} & \eta a_{62} & 0 & 0 & 0 & 0 \end{pmatrix} \tag{9}$$

The coefficients in the first two rows of the above two matrices follow:

$$(1 - \nu^2) a_{11} = \frac{1}{(1+p_1)^2} \left(\frac{1 + 2\varepsilon_1 - p_1}{1 + p_1} + \nu \frac{\varepsilon_2 - p_2}{1 + p_2} \right)$$

$$(1 - \nu^2) a_{21} = \frac{1 + \varepsilon_1}{(1+p_1)^2} + \nu \frac{1}{1 + p_2}$$

$$(1 - \nu^2) b_{11} = -\frac{1 + \varepsilon_1}{(1+p_1)^3} \left(\frac{1 + 3\varepsilon_1 - 2p_1}{1 + p_1} + 2\nu \frac{\varepsilon_2 - p_2}{1 + p_2} \right) \tag{10}$$

$$(1 - \nu^2) b_{21} = -\frac{1 + \varepsilon_1}{(1+p_1)^2} + \nu \frac{1 + \varepsilon_2}{(1+p_2)^2}$$

as well as

$$(1 - \nu^2) a_{22} = \frac{1}{(1+p_2)^2} \left(\frac{1 + 2\varepsilon_2 - p_2}{1 + p_2} + \nu \frac{\varepsilon_1 - p_1}{1 + p_1} \right)$$

$$(1 - \nu^2) a_{12} = \frac{1 + \varepsilon_2}{(1+p_2)^2} + \nu \frac{1}{1 + p_1}$$

$$(1 - \nu^2) b_{22} = -\frac{1 + \varepsilon_2}{(1+p_2)^3} \left(\frac{1 + 3\varepsilon_2 - 2p_2}{1 + p_2} + 2\nu \frac{\varepsilon_1 - p_1}{1 + p_1} \right) \tag{11}$$

$$(1 - \nu^2) b_{12} = -\frac{1 + \varepsilon_2}{(1+p_2)^2} + \nu \frac{1 + \varepsilon_1}{(1+p_1)^2}$$

The other coefficients are

$$a_{51} = C_{\eta 1} a_{\varepsilon 1}, \qquad a_{52} = C_{\eta 1} a_{\varepsilon 2},$$
$$a_{61} = C_{\eta 2} a_{\varepsilon 1}, \qquad a_{62} = C_{\eta 2} a_{\varepsilon 2}. \tag{12}$$

By means of the second Piola-Kirchhoff stress components with respect to intermediate configuration:

$$S_1 = \frac{E}{1 - \nu^2} \left(\frac{\varepsilon_1 - p_1}{1 + p_1} + \nu \frac{\varepsilon_2 - p_2}{1 + p_2} \right),$$

$$S_2 = \frac{E}{1 - \nu^2} \left(\frac{\varepsilon_2 - p_2}{1 + p_2} + \nu \frac{\varepsilon_1 - p_1}{1 + p_1} \right) \tag{13}$$

we have

$$a_{\varepsilon 1} = \frac{1}{\sqrt{6}} \frac{E}{1 - \nu^2} \frac{1}{1 + p_1} \frac{S_1(2 - \nu) + S_2(-1 + 2\nu)}{S_{eq}},$$

$$a_{\varepsilon 2} = \frac{1}{\sqrt{6}} \frac{E}{1 - \nu^2} \frac{1}{1 + p_2} \frac{S_2(2 - \nu) + S_1(-1 + 2\nu)}{S_{eq}},$$

$$a_{p 1} = -\frac{1}{\sqrt{6}} \frac{E}{1 - \nu^2} \frac{1 + \varepsilon_1}{(1 + p_1)^2} \frac{S_1(2 - \nu) + S_2(-1 + 2\nu)}{S_{eq}}, \tag{14}$$

$$a_{p 2} = -\frac{1}{\sqrt{6}} \frac{E}{1 - \nu^2} \frac{1 + \varepsilon_2}{(1 + p_2)^2} \frac{S_1(2 - \nu) + S_2(-1 + 2\nu)}{S_{eq}},$$

$$\delta_1 = \left[\frac{c_1}{3}(2S_1 - S_2) + \frac{c_2}{9}(2S_1^2 - 2S_1 S_2 - S_2^2) \right] \cdot J(0) \pi^\lambda \eta(S - Y),$$

$$\delta_2 = \left[\frac{c_1}{3}(2S_2 - S_1) + \frac{c_2}{9}(2S_2^2 - 2S_1 S_2 - S_1^2) \right] \cdot J(0) \pi^\lambda \eta(S - Y). \tag{15}$$

With all the above quantities we have finally

$$C_{\eta 1} = \frac{\delta_1(1 + p_1)}{1 - a_{p_1}\delta_1(1 + p_1) - a_{p_2}\delta_2(1 + p_2)},$$

$$C_{\eta 2} = \frac{\delta_2(1 + p_2)}{1 - a_{p_1}\delta_1(1 + p_1) - a_{p_2}\delta_2(1 + p_2)}, \tag{16}$$

such that (12) are explained.

4   Numerical analysis of wave equations

The numerical analysis of the governing equations has been performed for a quadratic thin plate geometry and diverse boundary and initial conditions. Through the study of Equation (2), we would like to investigate whether a soliton-type solution can be constructed, and which physical meaning a solution of this kind may have in the description of the considered physical system.

4.1   Multigrid-methods

The performance of numerical schemes for solving complicated partial differential equations can be strongly improved by using a hierarchy of grids that cover the computational domain Ω. On these grids, the PDEs are discretized, and a system of linear equations is obtained for each grid. In general, this linear system can be written as $Au = f$, where A is the discretization matrix, u is the vector of unknowns, and f is the vector of known quantities. Depending on the discretization technique, and the numerical procedure (for example, Finite Volumes Method), the matrix A results to be *sparse*, this meaning that its nonzero entries are few. The "sparseness" of A is a desirable property because it can be proven to improve the computational efficiency.

Consider as an example the case in which only two grids are used. In order to solve the system of equations $Au = f$ on the fine grid, multigrid solvers are applied. In general, for a given initial trial solution, u^0, the initial defect, $Au^{(0)} - f$, posses a wide frequency spectrum in Fourier space.

A multigrid solver solves the problem $Au = f$ iteratively, and consists of two "components" called *smoother*, and *coarse-grid corrector*, respectively. The *smoother* reduces the higher frequencies of the defect. By applying the smoother, S, a certain number of times (for example, ν times, with $\nu = 3$), the smoothed defect $AS^v u^{(i)} - f$ can be approximated on the coarse grid.

At this stage, the coarse-grid corrector is introduced: the smoothed defect is restricted to the coarse grid, and the corresponding linear

system is solved. The obtained solution is then prolongated to the fine grid, and the result is used as a correction. This procedure reduces the lower frequencies of the defect. Finally, the smoother is applied again in order to obtain the updated solution. In formulae, the above method can be as follows described:

$$
\begin{aligned}
u^{(i+1)} &= S^\nu \left(S^\nu u^{(i)} - pA_c^{-1} r(A_f S^\nu u^{(i)} - f_f) \right) \\
&= S^\nu (I - pA_c^{-1} r A_f) S^\nu u^{(i)} + pA_c^{-1} r f_f,
\end{aligned}
\tag{17}
$$

where A_f and A_c denote the matrices on the fine and coarse gride, respectively, f_f is the right hand side on the fine grid, S is the smoother, p is the prolongation and r denotes the restriction operator. Some other details are given in [5].

4.2   UG-code

UG stands for "unstructured grids". This is a flexible software tool for solving partial differential equations. It contains a grid manager, which is designed for generating unstructured locally refined grids in two and three dimensions. Its data structure allows for a fast implementation of various discretizations though many standard discretizations like finite volumes and finite elements can already be found as examples. With the implemented discretization, UG is capable of generating a system of linear equations. For solving the system a whole range of robust and efficient algorithms is already available including several multigrid methods. UG can also be used on highly parallel supercomputers. Hence, even very large systems of linear equations can be solved by using UG. Further information can be found at [6].

5   Preliminary simulation results

As a first step in a numerical analysis of diverse elasto-viscoplastic stress-strain histories we consider here only elastic waves but in two elastic ranges:

- the initial elastic range "A" with $p_1 = p_2 = 0$

- a subsequent elastic range "B" with $p_1 = 0.2$, and $p_2 = 0.1$.

For convenience the non-dimensional time is introduced by means of $\tau \equiv t/T$ where $T = 10^{-3}\,s$ as well as the non-dimensional $X_A = \psi_A/L_A$, $A \in \{1, 2\}$ where dimensions of the gage square (cf. Fig. 1)are $L_1 = L_2 = 2\,cm$. In this way $\tau \in [0, 1]$ and $X_A \in [-1/2, 1/2]$. Under these assumptions only the following two wave equations are non-trivial:

$$\frac{\partial^2 U_A}{\partial \tau^2} = \frac{1}{\rho_0} \left(\frac{T}{L_A} \right)^2 \frac{\partial}{\partial X_A} \left[\frac{1 + \varepsilon_A}{(1 + p_A)^2} S_A \right], \tag{18}$$

where S_1, S_2 are given by (13).

Moreover in all the loading histories the initial velocities on the gage square edges are such that $V_2^* = 0.5\,V_1^*$.

5.1 Symmetric initial and boundary conditions

Initial conditions

$$\mathbf{U}(X_1, X_2, t = 0) = \mathbf{0},$$

$$\frac{\partial \mathbf{U}}{\partial t}(X_1 = \pm 1/2, X_2, t = 0) = \pm V_1^* \mathbf{e}_1,$$

$$\frac{\partial \mathbf{U}}{\partial t}(X_1, X_2 = \pm 1/2, t = 0) = \pm V_2^* \mathbf{e}_2, \tag{19}$$

$$\frac{\partial \mathbf{U}}{\partial t}(-1/2 < X_1 < 1/2, -1/2 < X_2 < 1/2, t = 0) = \mathbf{0},$$

where $\mathbf{U} = \sum_{\alpha=1}^{3} U_\alpha \mathbf{e}_\alpha$ is the displacement vector, and $\{\mathbf{e}_\alpha\}_{\alpha=1}^{3}$ are the unit vectors of the canonical base in $\mathbb{R}^3$.
Boundary conditions

$$\sigma_{\alpha\beta}(X_1 = \pm 1/2, X_2, t) = 0,$$

$$\sigma_{\alpha\beta}(X_1, X_2 = \pm 1/2, t) = 0, \quad (\alpha, \beta = 1, 2, 3). \tag{20}$$

5.1.1   Case A$_2$-symmetric

It refers to wave propagation within the initial elastic range where the plastic strain vanishes. The displacements U_1 and U_2 in the Figure 2 have an oscillating time behaviour with many intersections. Initially, each function shows a wide oscillation, followed by a small *plateaux*. Afterwards the behaviour becomes more regular. The peaks decrease and increase their amplitude in a periodic way.
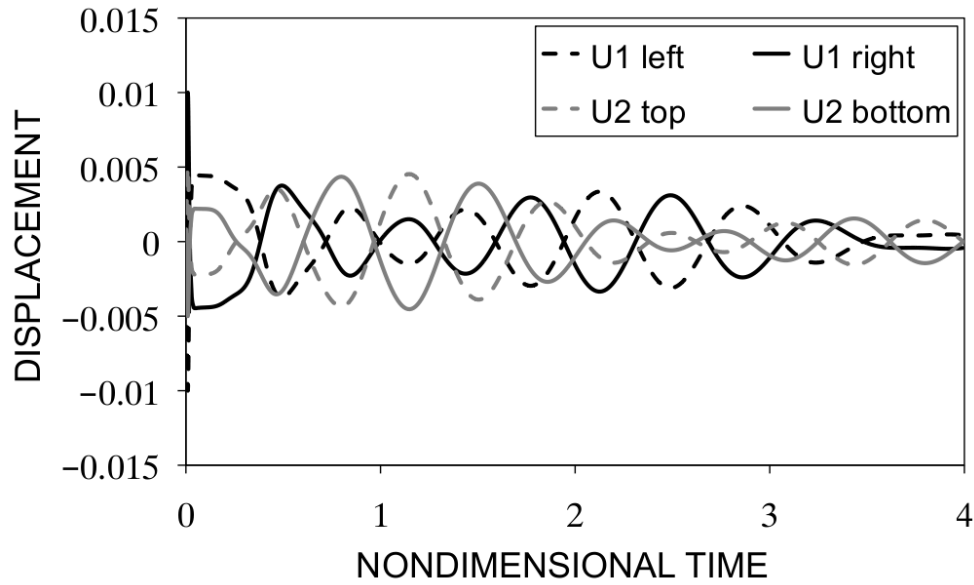

Figure 2: Time evolution of the displacements U_1 and U_2, computed at the left, right, top, and bottom midpoints at boundaries of the domain.

Six characteristic spatial distributions within the considered square plate are depicted in the following figure.

- The magnitude of the displacement U_1 in the Figure 3(a) is maximal at the left and right boundary and null at the origin of the domain. At both the left- and right-hand-side, the iso-displacements lines are sparse, and show comparatively large variations of curvature. They become more densely packed and

converge to straight lines as soon as the centre of the domain is approached.

In the spatial distribution of U_2 at the same time, we see that two main areas can be detected, in which the global minimum and maximum of U_2 are attained (cf. Figure 3(b)).

- Looking at the Figure 3(c) we note that eight symmetric regions can be detected. At this time, six "bubble"-like areas are being formed.

  At the same time, the global minumum and maximum of U_2 move towards the upper and lower boundary of the domain (cf. Figure 3(d)).

- Finally, in Figure 3(e), eigth regions for U_1 can be distinguished. At the top and bottom of the domain, two "bubbles" are being formed, while on the left- and right-hand-side, the "bubbles" tend to merge in order to form a single bubble.

  The global minumum and maximum of U_2 at this time tend to move again towards the centre of the domain (cf. Figure 3(f)).

The magnitude of the displacement increases from the blue region towards the red one. The iso-displacement lines describe a spatial symmetric situation in which the changes in curvature (sometimes quite abrupt) are due to the interaction between the deformations ε_1 and ε_2.
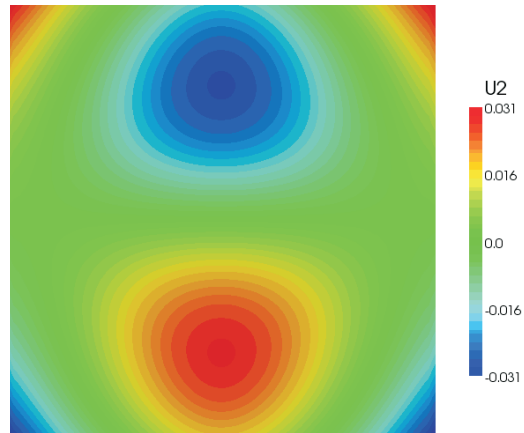
(a) Snapshot of the space behaviour of U_1 at time $\tau = 0.22$.
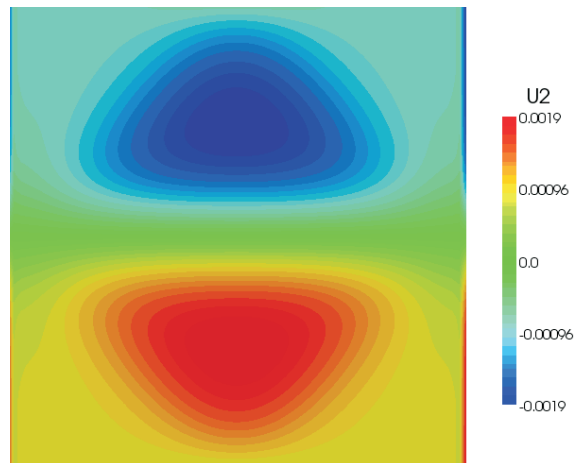
(b) Snapshot of the space behaviour of U_2 at time $\tau = 0.22$.
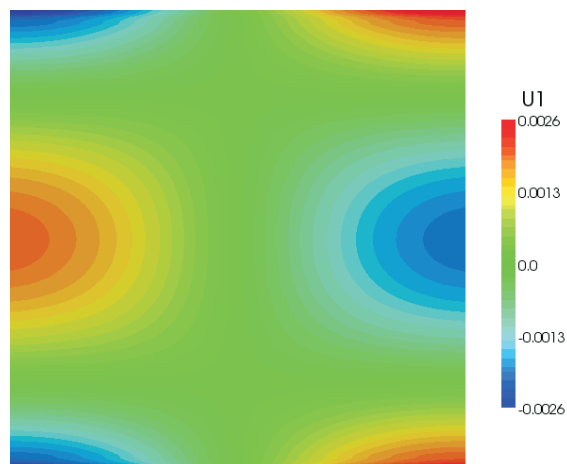
(c) Snapshot of the space behaviour of U_1 at time $\tau = 1.48$.
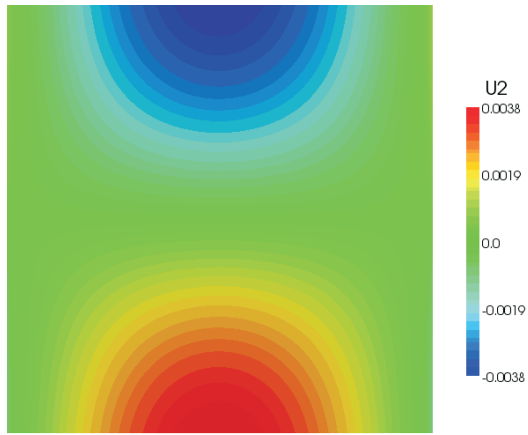
(d) Snapshot of the space behaviour of U_2 at time $\tau = 1.48$.
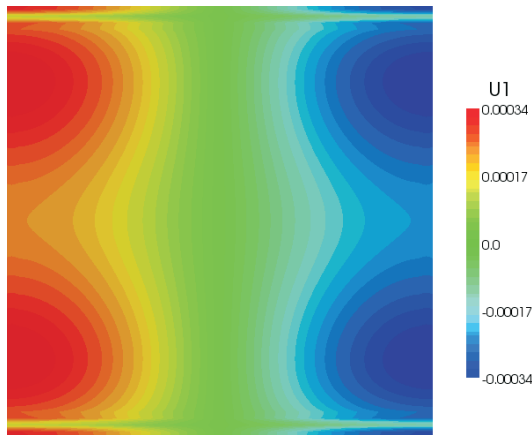
(e) Snapshot of the space behaviour of U_1 at time $\tau = 3.53$.
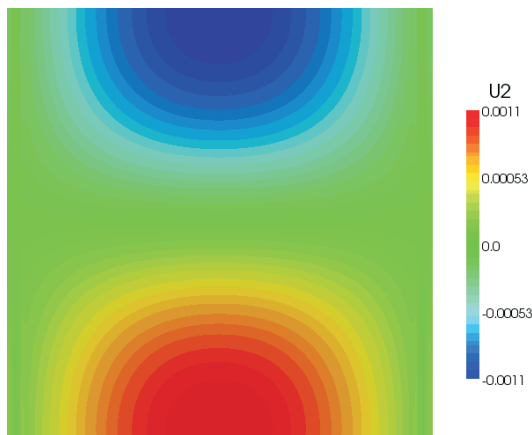
(f) Snapshot of the space behaviour of U_2 at time $\tau = 3.53$.

Figure 3: Case A_2 for symmetric boundary conditions.

5.1.2   Case B$_2$-symmetric

It refers to the same boundary conditions as the previous case but with the essential difference that plastic strain is constant and different from zero. In other words, we have also elastic behaviour, but previous plastic strains acquired by some "static" (i.e. slow) straining have finite non-zero value, which does not change in the course of wave propagation. Here we deal with so-called *subsequent elastic range.*

From Figure 4 we see that the displacements U_1 and U_2 have an oscillating time behaviour. Only the curves showing the time behaviour of the displacement U_2 feature with some intersections when $\tau \in [0, 2[$. Within the studied time interval, no *plateaux* is observed.
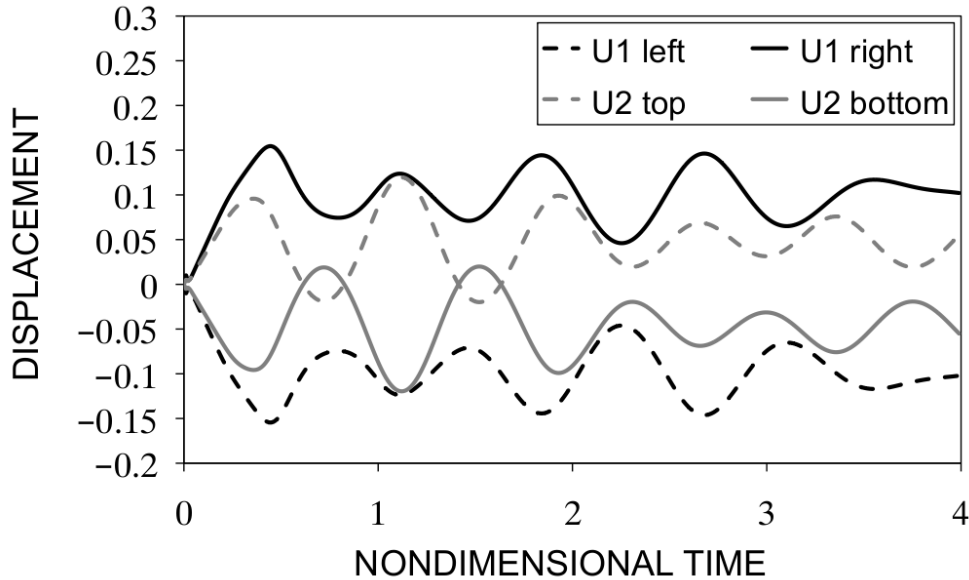
Figure 4: Time evolution of the displacements U_1 and U_2, computed at the midpoints of left, right, top, and bottom boundaries of the domain.

Again we use only six pictures to illustrate the whole time history.

The magnitude of the displacement increases from the blue region towards the red one. The iso-displacement lines describe a spatial symmetric situation (cf. Figure 5).

(a) Snapshot of the space behaviour of U_1 at time $\tau = 0.52$.
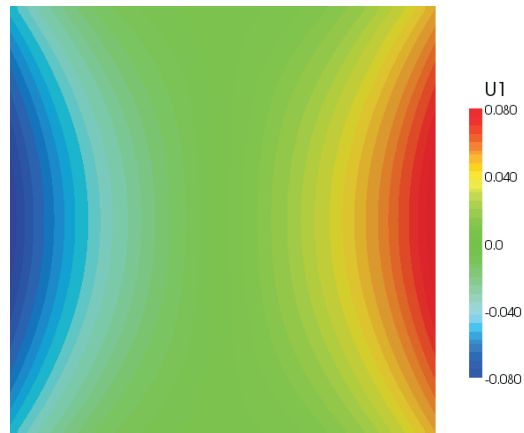

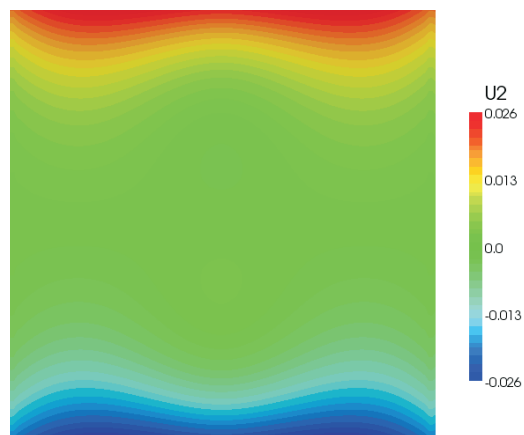(b) Snapshot of the space behaviour of U_2 at time $\tau = 0.52$.
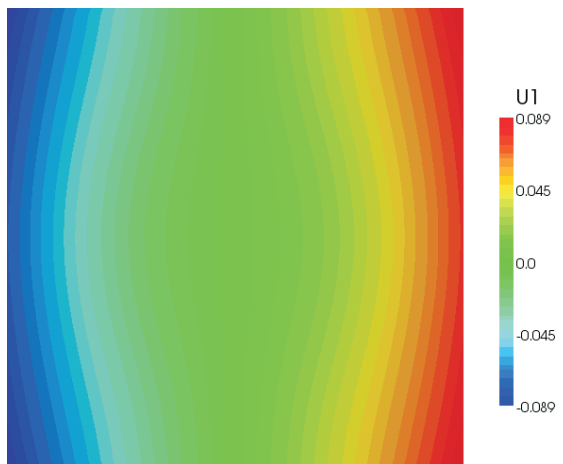
(c) Snapshot of the space behaviour of U_1 at time $\tau = 0.75$.

(d) Snapshot of the space behaviour of U_2 at time $\tau = 1.48$.

(e) Snapshot of the space behaviour of U_1 at time $\tau = 0.88$.

(f) Snapshot of the space behaviour of U_2 at time $\tau = 0.88$.

Figure 5: Case B_2 for symmetric boundary conditions.

We also computed the displacements U_1 and U_2 for different values of the parameter k. The dependence of the response angle $\arctan(U_2/U_1)$ on the initial phase $\arctan(V_2/V_1)$ is shown in Figure 5.2.2.

5.2 Non-symmetric initial and boundary conditions

Initial conditions

$$\mathbf{U}(X_1, X_2, 0) = 0,$$

$$\frac{\partial \mathbf{U}}{\partial t}(X_1 = 1/2, X_2, t = 0) = V_1^* \mathbf{e}_1,$$

$$\frac{\partial \mathbf{U}}{\partial t}(X_1 = -1/2, X_2, t = 0) = \mathbf{0},$$

$$\frac{\partial \mathbf{U}}{\partial t}(X_1, X_2 = 1/2, t = 0) = V_2^* \mathbf{e}_2, \tag{21}$$

$$\frac{\partial \mathbf{U}}{\partial t}(X_1, X_2 = -1/2, t = 0) = \mathbf{0},$$

$$\frac{\partial \mathbf{U}}{\partial t}(X_1 < 1/2, X_2 < 1/2, t = 0) = 0.$$

Boundary conditions

$$\mathbf{U}(X_1 = -1/2, X_2, t) = \mathbf{0},$$

$$\mathbf{U}(X_1, X_2 = -1/2, t) = \mathbf{0},$$

$$\boldsymbol{\sigma}(X_1, X_2 = 1/2, t) = \mathbf{0}, \tag{22}$$

$$\boldsymbol{\sigma}(X_1 = 1/2, X_2, t) = \mathbf{0}.$$

5.2.1 Case $\mathbf{A}_2$ non-symmetric

We are dealing now with the initial elastic range again. Boundary conditions are now changed in such a way that left and bottom edges are fixed whereas the other initial conditions are the same. Since the loading is non-symmetric, displacements of the single mid-point of the square suffice our purpose.
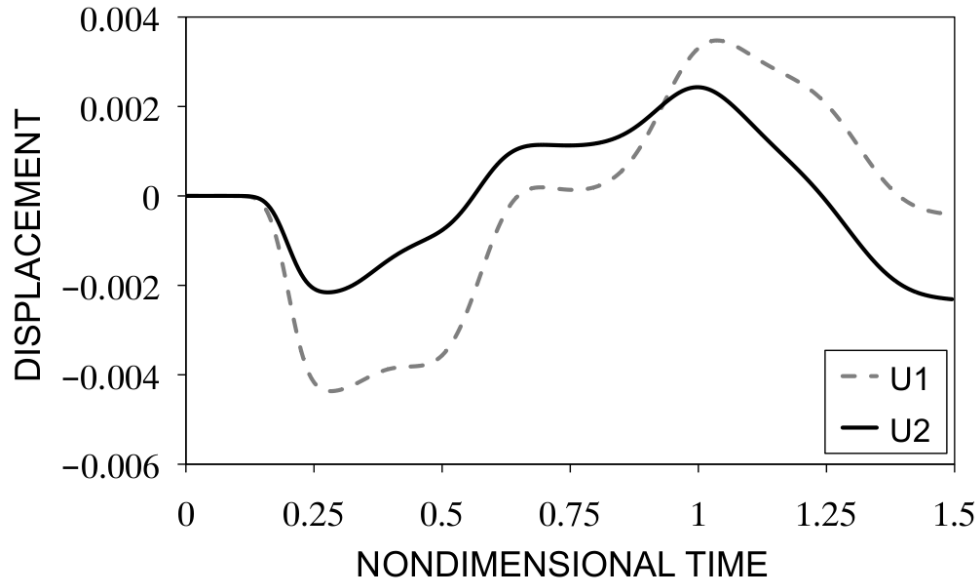
Figure 6: Time evolution of the displacements U_1 and U_2, computed at the centre of the domain.

The displacements $U_1(X_1 = \frac{1}{2}, X_2 = \frac{1}{2}, \tau)$ and $U_2(X_1 = \frac{1}{2}, X_2 = \frac{1}{2}, \tau)$ are both zero and have zero derivative at $\tau = 0$. Until $\tau = 0.8$, they seem to be synchronized. After the intersection, synchronization is lost, and a delay between U_1 and U_2 can be observed. U_2 seems to be "faster" than U_1 until the second intersection occurs (cf. Figure 6).

The following six "snapshots" are chosen from the current history.

The magnitude of the displacement increases from the blue region towards the red one. The iso-displacement lines describe a spatial asymmetric situation in which the changes in curvature (sometimes quite abrupt) are due to the interaction between the deformations ε_1 and ε_2. (cf. Figure 7)
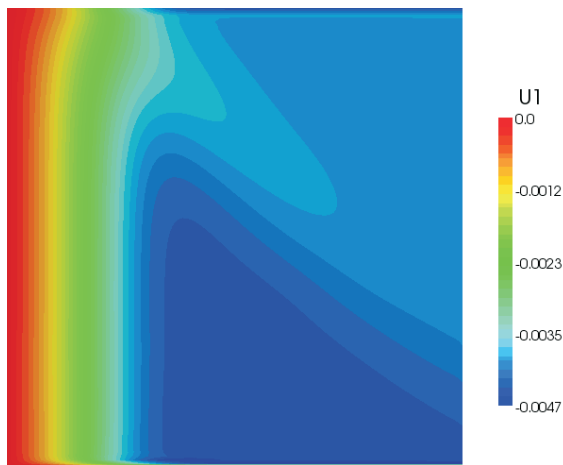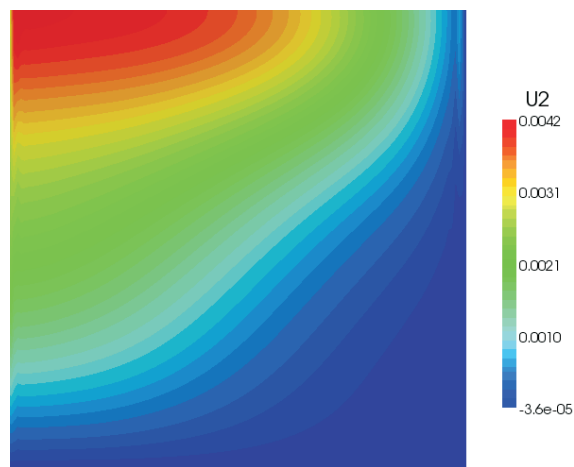
(a) Snapshot of the space behaviour of U_1 at time $\tau = 0.325$.
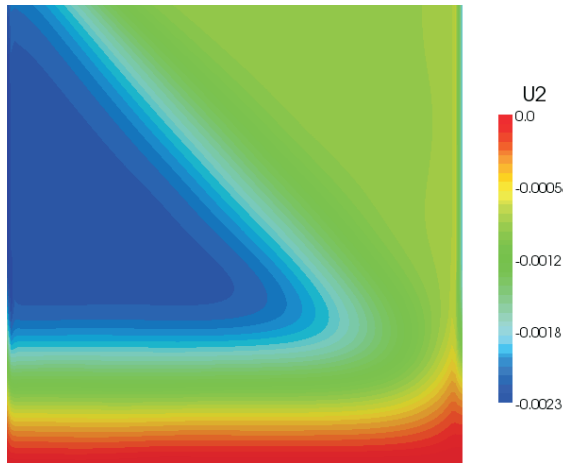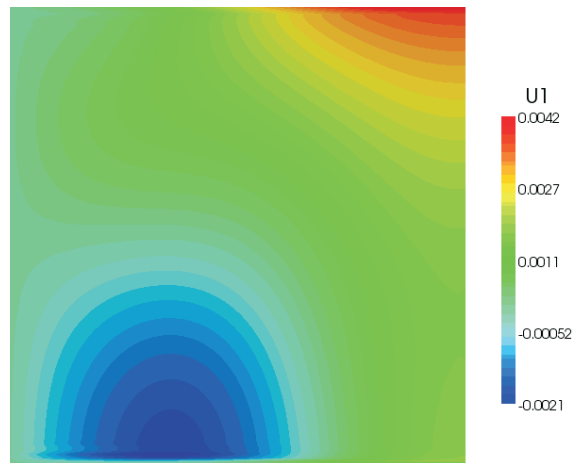

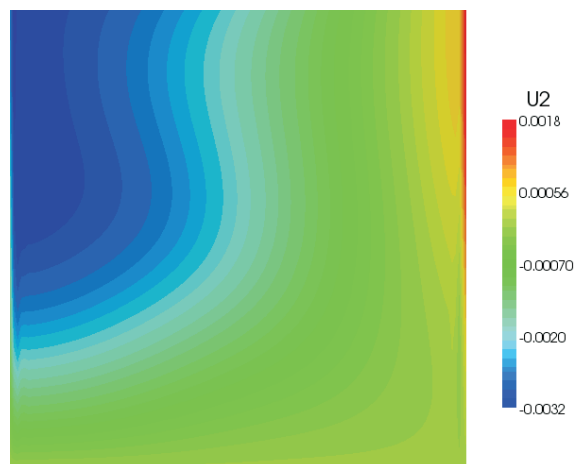(b) Snapshot of the space behaviour of U_2 at time $\tau = 0.325$.
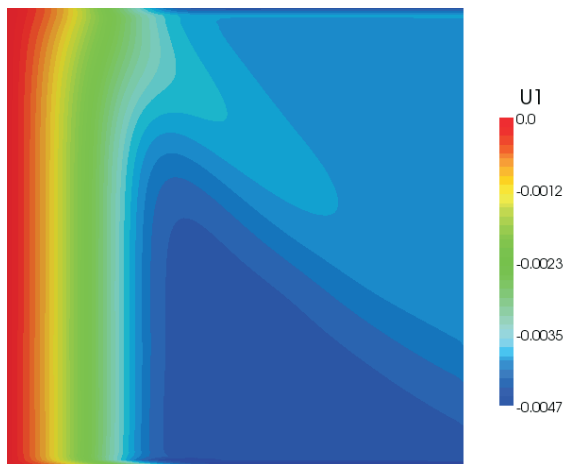
(c) Snapshot of the space behaviour of U_1 at time $\tau = 0.82$.

(d) Snapshot of the space behaviour of U_2 at time $\tau = 0.82$.

(e) Snapshot of the space behaviour of U_1 at time $\tau = 1.38$.

(f) Snapshot of the space behaviour of U_2 at time $\tau = 1.38$.

Figure 7: Non-symmetric case A_2

5.2.2   Case B_2 non-symmetric

In the last considered non-symmetric case the initial conditions again include $p_1 = 0.2$, $p_2 = 0.1$.

The displacements $U_1(X_1 = 0, X_2 = 0, \tau)$ and $U_2(X_1 = 0, X_2 = 0, \tau)$ are both zero and have zero derivative at $\tau = 0$. The two functions are synchronized on a small interval before intersection occurs. Afterwards delay is observed. The magnitude of displacement U_2 is smaller than that of U_1 (cf. Figure 8).
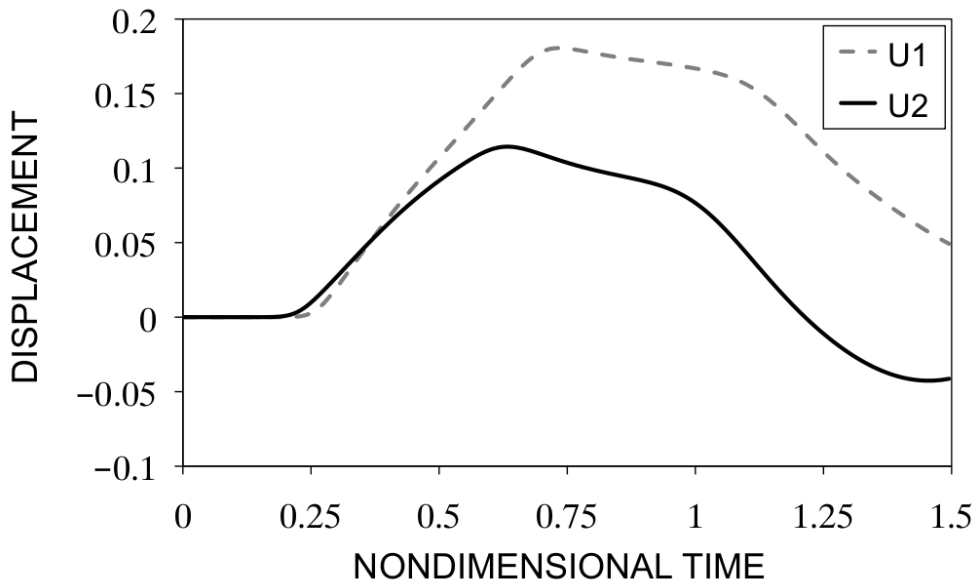

Figure 8: Non-symmetric case B_2 - time plots of displacements U_1 and U_2 computed at the centre of the domain.

The other six characteristic plots are organized in the same way as above. The magnitude of the displacement increases from the blue region towards the red one. The iso-displacement lines describe a spatial asymmetric situation. The curvature of the isolines varies more smoothly both in time and in space than in the previous case (cf. Figure 9). This could be due to a smoothing effect of the plastic deformation.

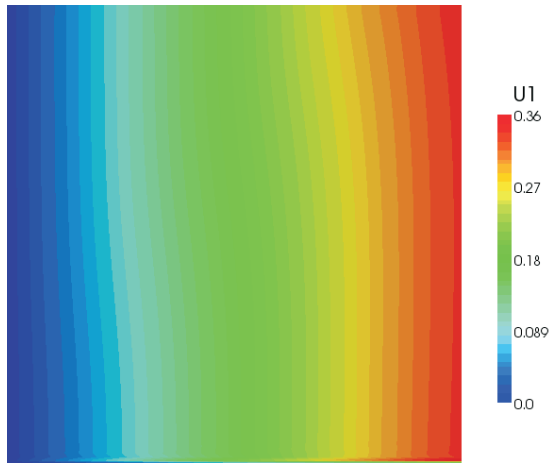(a) Snapshot of the space behaviour of U_1 at time $\tau = 0.44$.

(b) Snapshot of the space behaviour of U_2 at time $\tau = 0.44$.
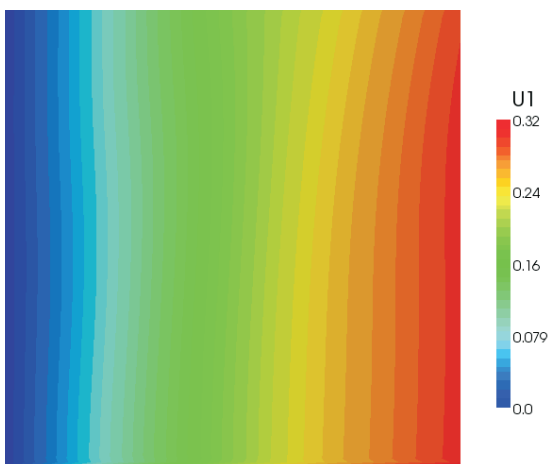
(c) Snapshot of the space behaviour of U_1 at time $\tau = 0.75$.

(d) Snapshot of the space behaviour of U_2 at time $\tau = 1.48$.

(e) Snapshot of the space behaviour of U_1 at time $\tau = 0.88$.

(f) Snapshot of the space behaviour of U_2 at time $\tau = 0.88$.
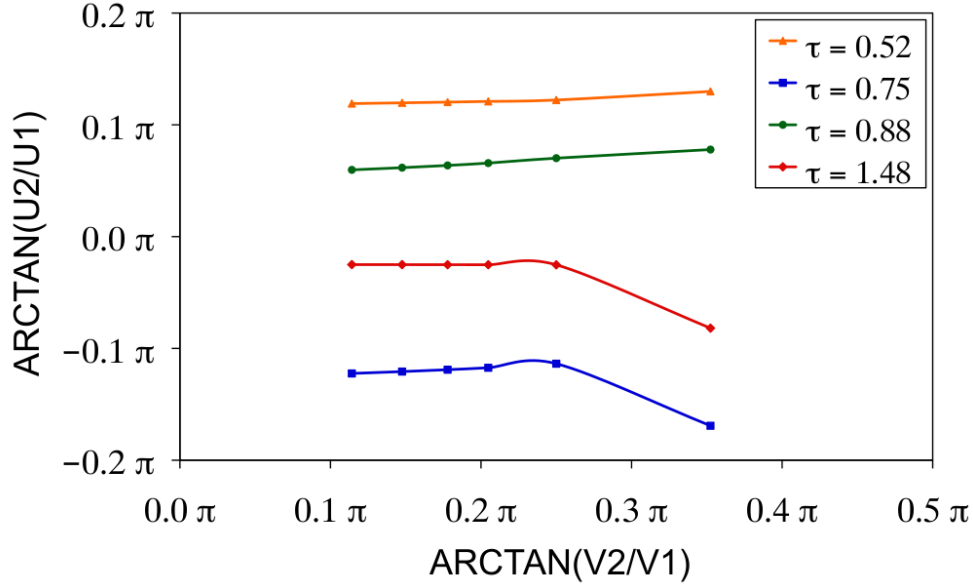
Figure 9: Non-symmetric case B_2

Figure 10: Plot of $\arctan(U_2/U_1)$ as a function of $\arctan(V_2/V_1)$ at different times.

6   Conclusion

The problem of two-dimensional plastic waves of QRI viscoplastic materials is properly formulated. A simplest non-linear evolution equation for plastic stretching is used. Wave equations are stated together with boundary and initial conditions as well as momentum equations.

In the preliminary analysis, characteristic for initial and subsequent elastic ranges it was taken direction of (elastic) 2-D wave does not change during propagation. The results hold also for non-proportional elastic paths. They are useful for the subsequent analysis of plastic waves when plastic strains are small and comparable with elastic ones.

At this stage of research, it is easier to speak about prospective research. The numerical code is now tested and prepared for real plastic waves when proportional as well as non-proportional stress-strain

histories take place. Thus, a limited program would include (a) diverse stress directions at proportional histories; (b) nonproportional stress histories with previous static plastic straining; (c) investigation whether it is possible to split plastic waves into two principal directions; (d) a special case when plastic and total strains are much larger than elastic ones.

References

[1] M.Micunovic, C.Albertini, P.Pino and G.Maresca, Some results concerning damage acquired by cruciform Hopkinson bar technique. W.K.Nowacki and H.Zhao eds. *Proc. 10th EMMC10* , Kazimerz Dolny, Poland, 185-194 ,2007.

[2] M.Micunovic and A.Baltov, Plastic wave propagation in Hopkinson bar – revisited, *Archives of Mechanics*, **54/5-6**, 577-602, 2002.

[3] M.Micunovic, C.Albertini and M.Montagnani, High strain rate viscoplasticity of AISI 316 stainless steel from tension and shear experiments. P.Miljanic ed. *Solid Mechanics - Serbian Acad. Sci.-Sci. Meetings* ,**87/3**, 97-106, 1997.

[4] W.K.Nowacki, *Stress Waves in Non-Elastic Solids*, Pergamon, Oxford, 1978.

[5] W. Hackbusch. *Multi-Grid Methods and Applications*. Springer Series in Computational Mathematics, 1985.

[6] P. Bastian, K. Birken, K. Johannsen, S. Lang, N. Neuss, H. Rentz-Reichert and C. Wieners. UG - A Flexible Software Toolbox for Solving Partial Differential Equations. *Computing and Visualization in Science* **1**, 27-40, 1997.

Dvodimenzioni plastični talasi u QRI viskoplastičnim materialima

Predmet ovog rada je analiza talasa koji se pojavljuju tokom eksperimenta sa dvoosnim Hopkinsonovim štapom kada se taj uredjaj sastoji iz krstastog zateznog uzorka oivičenog sa četiri veoma duga elastična štapa. Nasuprot uobičajene analize koja pokušava da izvuče zaključke iz ponašanja elastičnih štapova mi ovde uzimamo u obzir realne plastične talase unutar uzorka sa nekoliko stotina odbijanja. Primenjeni su konstitutivni model prividno nezavisan od brzine kao i opštiji model sa tenzorskom funkcijom na čelik ASME 537. Analiziraju se takodje i plastične brzine talasa nepostojeće u tradicionalnoj elasto-viskoplastičnosti. Dati su neki uvodni numerički rezultati za simetrične i nesimetrične slučajeve opterećenja u početnim i sledećim elastičnim opsezima.